



Calcium–bismuth electrodes for large-scale energy storage (liquid metal batteries)



Hojong Kim, Dane A. Boysen¹, Takanari Ouchi, Donald R. Sadoway*

Department of Materials Science and Engineering, Massachusetts Institute of Technology, 77 Massachusetts Avenue, Cambridge, MA 02139-4307, United States

HIGHLIGHTS

- Electrochemical behavior of Ca–Bi alloys is investigated for liquid metal batteries.
- Electrochemical set-up is developed for calcium as the electro-active species (itinerant ion).
- Ca–Bi electrodes exhibit chemically reversible reactions and high coulombic efficiency.
- Electrode overpotential of Ca–Bi alloys is investigated in terms of charge transfer and mass transport.
- Co-deposition of Ba from the electrolyte improved the electrode performance.

ARTICLE INFO

Article history:

Received 23 January 2013

Received in revised form

9 April 2013

Accepted 11 April 2013

Available online 19 April 2013

Keywords:

Liquid metal batteries

Molten salts

Ca alloys

Ca–Bi alloys

Liquid alloys

Molten salt electrochemistry

ABSTRACT

Calcium is an attractive electrode material for use in grid-scale electrochemical energy storage due to its low electronegativity, earth abundance, and low cost. The feasibility of combining a liquid Ca–Bi positive electrode with a molten salt electrolyte for use in liquid metal batteries at 500–700 °C was investigated. Exhibiting excellent reversibility up to current densities of 200 mA cm^{−2}, the calcium–bismuth liquid alloy system is a promising positive electrode candidate for liquid metal batteries. The measurement of low self-discharge current suggests that the solubility of calcium metal in molten salt electrolytes can be sufficiently suppressed to yield high coulombic efficiencies >98%. The mechanisms giving rise to Ca–Bi electrode overpotentials were investigated in terms of associated charge transfer and mass transport resistances. The formation of low density Ca₁₁Bi₁₀ intermetallics at the electrode–electrolyte interface limited the calcium deposition rate capability of the electrodes; however, the co-deposition of barium into bismuth from barium-containing molten salts suppressed Ca–Bi intermetallic formation thereby improving the discharge capacity.

© 2013 Elsevier B.V. All rights reserved.

1. Introduction

The alkaline-earth metal calcium ranks fifth among the most-abundant elements in the earth's crust, just after iron [1]. As the demand for ultra-low cost grid-scale energy storage increases, this earth-abundant and low cost metal invites scrutiny as an attractive electrode material for liquid metal battery energy storage. Liquid metal batteries comprise two liquid metal electrodes separated by a molten salt electrolyte that self-segregate into three liquid layers based upon density and immiscibility. Despite the popularity of

lithium-based systems for electrochemical energy storage, recent thermodynamic and economic analyses of various liquid metal battery electrode couples indicate that calcium-based systems have higher equilibrium cell voltages and lower costs than comparable lithium systems [2]. The high reactivity and strong reducing power of calcium combined with its high solubility in molten salts disqualify the metal as an electrode. Instead, the primary use of calcium has been restricted to the extraction and refining of less reactive metals such as titanium, zirconium, and rare earth elements [1].

Historically, two types of high temperature batteries using calcium as the active component have been developed: thermally activated reserve batteries (or thermal batteries) and secondary calcium-metal sulfide batteries. In thermal battery systems, elemental solid calcium negative electrodes were used with transition metal oxide positive electrodes (K₂Cr₂O₇, CaCr₂O₇, or WO₃), and a molten salt electrolyte (LiCl–KCl). The cell reactions in a

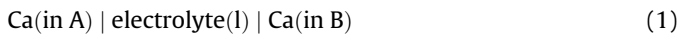
* Corresponding author. Tel.: +1 617 253 3487; fax: +1 617 253 5418.

E-mail addresses: hojong@mit.edu (H. Kim), dane.boysen@hq.doe.gov (D.A. Boysen), t_ouchi@mit.edu (T. Ouchi), dsadoway@mit.edu (D.R. Sadoway).

¹ Present address: Advanced Research Projects Agency-Energy, U.S. Department of Energy, 1000 Independence Avenue SW, Washington, DC 20585, United States.

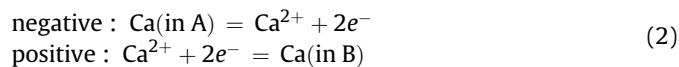
thermal battery are complex and involve direct chemical reactions between the electrodes and the electrolyte that make it impossible to recharge the cell. These calcium-based thermal batteries were used in military applications such as missiles, ordnances, and nuclear weapons until the 1980s [3]. In the late 1970s, Argonne National Laboratory began developing calcium-metal sulfide batteries with solid calcium alloy negative electrodes (Ca–Al, Ca–Mg, or Ca–Si), metal sulfide positive electrodes (FeS₂, FeS, NiS, or CoS), and a molten salt electrolyte (LiCl–NaCl–CaCl₂–BaCl₂) for electric vehicle applications [4–6]. However, these efforts were discontinued as attention shifted to higher energy density lithium-based battery chemistries.

In this study, we investigate the possibility of using calcium-based liquid alloys as electrodes in liquid metal batteries for grid-scale electrochemical energy storage. The prototypical calcium-based liquid metal battery cell can be written as:



where A (e.g.; Mg, Zn, or Al) is the negative electrode host metal, and B is the positive electrode metal (e.g.; Bi, Sb, Sn, or Pb). Due to the high melting temperature of calcium (842 °C), alloying with more noble A metals is desired to lower the melting point of the negative electrode and minimize side reactions with the molten salt electrolyte. The electrolyte can be a molten mixture of alkali and/or alkaline-earth halide salts; which typically have high ionic conductivities of greater than 1 S cm^{−1}.

For this cell, the generic half-cell reactions are



and the overall cell reaction is



The thermodynamic driving force for this reaction is supplied by the change in partial molar Gibbs free energy of the cell,

$$\Delta \bar{G}_{\text{cell}} = \bar{G}_{\text{Ca(in B)}} - \bar{G}_{\text{Ca(in A)}} \quad (4)$$

where the partial molar Gibbs energy \bar{G}_i for each component i is given by

$$\begin{aligned} \bar{G}_{\text{Ca(in B)}} &= G_{\text{Ca}}^\circ + RT \ln a_{\text{Ca(in B)}} \\ \bar{G}_{\text{Ca(in A)}} &= G_{\text{Ca}}^\circ + RT \ln a_{\text{Ca(in A)}} \end{aligned} \quad (5)$$

where a_i is the activity, G_{Ca}° the standard chemical potential of calcium, R the gas constant, and T the temperature. The change in partial molar Gibbs free energy can be related to a cell equilibrium voltage $E_{\text{cell,eq}}$ by the Nernst equation

$$\Delta \bar{G}_{\text{cell}} = -zFE_{\text{cell,eq}} \quad (6)$$

where $z = 2$ is the number of electrons exchanged in the reaction and F is the Faraday constant. From Equations (4)–(6), the cell equilibrium voltage is related to the activities of calcium in the positive and negative electrodes:

$$E_{\text{cell,eq}} = -\frac{\Delta \bar{G}_{\text{cell}}}{zF} = -\frac{RT}{zF} \ln \left(\frac{a_{\text{Ca(in B)}}}{a_{\text{Ca(in A)}}} \right). \quad (7)$$

Conceptually, the thermodynamic driving force for cell discharge can be interpreted as a stronger interaction of calcium with metal B than metal A, where low calcium activity in metal B

and high calcium activity in metal A yields a high equilibrium cell voltage. In the present study, the feasibility of a calcium-based liquid metal battery is investigated using a liquid bismuth positive electrode ($B = \text{Bi}$); which has a low melting temperature (271 °C) and is minimally corrosive to typical cell construction materials at elevated temperatures, such as steels.

Previous thermodynamic investigations of Ca–Bi alloys led to the development of a highly stable reference electrode; which made the evaluation of the electrochemical performance of calcium-based liquid metal alloys in this study possible [7,8]. Those emf concentration cell studies employed a CaF₂ solid electrolyte with low electrical conductivity, i.e., 4.4×10^{-7} to 1.8×10^{-4} S cm^{−1} at 500–700 °C [9]; a value sufficient for thermodynamic investigations, but impractical for electrochemical energy storage applications. Molten salt electrolytes typically exhibit much higher conductivities (~ 1 S cm^{−1}); however, the solubility of calcium in molten salt electrolytes and resulting electronic conductivity make accurate electrochemical measurements experimentally difficult.

The following dissolution mechanism of calcium metal into a molten salt solution was proposed [10]:



where calcium metal reacts with Ca²⁺ cations to form subvalent species Ca₂⁺ or Ca⁺. In general, the solubility of calcium in molten salt electrolytes is reduced at lower temperatures and lower calcium activities in host metal electrodes. Previous research efforts measured pure calcium metal solubility in CaCl₂(l) to be 2.7–5.7 mol% at 820–1000 °C [11–13]. By contrast, Sharma [10] found that by alloying with another metal, the solubility of calcium can be significantly reduced to as low as 0.3 mol% calcium in CaCl₂(l) using a Ca–Cu alloy (30–70 mol%) electrode. Ukshe and Bukun [12] showed that the solubility of magnesium in MgCl₂(l) at 800 °C could be decreased by varying degrees by mixing the molten salt with other cation chloride salts, such as LiCl, NaCl, and BaCl₂, depending on the ionic size of the foreign cation species.

To suppress calcium dissolution in this study, low melting point electrolyte compositions were formulated with metal chlorides of less noble metals. Specifically, two compositions were selected: LiCl–NaCl–CaCl₂ (38–27–35 mol%, $T_m = 450$ °C) and LiCl–NaCl–CaCl₂–BaCl₂ (29–20–35–16 mol%, $T_m = 390$ °C) [4]. The physical and electrical properties of these are given in Table 1.

Two-phase metal alloys can serve as stable, consistent reference electrodes for highly reactive systems. For example, two-phase Li–Al alloys comprising Al(s) and LiAl(s) are commonly used as reference electrodes in lithium-bearing molten salt electrochemical cells due to the invariance of the equilibrium electrode potential with compositional changes within the two-phase regime [14]. Based upon these findings, a Ca–Bi alloy (calcium mole fraction $x_{\text{Ca}} = 0.35$) with low calcium activity ($a_{\text{Ca}} = 9 \times 10^{-10}$ at 600 °C) and solid–liquid (Ca₁₁Bi₁₀ + l) two-phase phase behavior (see Fig. 1)

Table 1
Physical and electrical properties of electrolytes.

Electrolyte	Composition/mol%	$T_{\text{liquidus}}/^\circ\text{C}$	$\rho^b/\text{g cm}^{-3}$	$\sigma^b/\Omega^{-1} \text{cm}^{-1}$	$T/^\circ\text{C}$
LiCl–NaCl–CaCl ₂	38–27–35	450 ^a	1.90	2.18	500
			1.85	2.58	600
			1.81	2.94	700
LiCl–NaCl–CaCl ₂ –BaCl ₂	29–20–35–16	390	2.29	1.56	500
			2.24	1.88	600
			2.19	2.19	700

^a Liquidus temperature estimated from the differential scanning calorimetry (DSC) at different heating rates.

^b Density and electrical conductivity at given temperature was approximated from pure components.

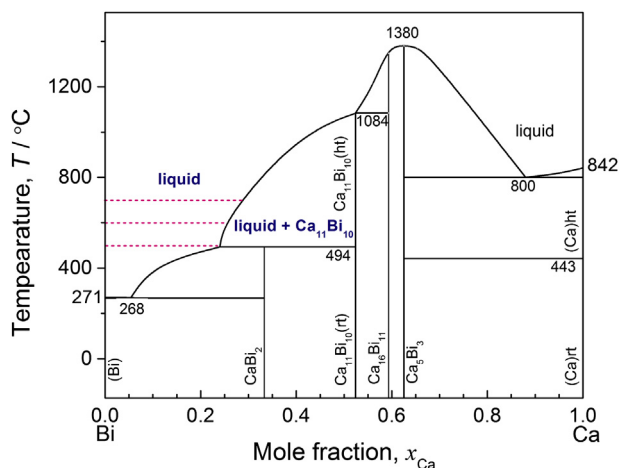


Fig. 1. Calcium–bismuth binary phase diagram [8] indicating composition range and temperatures of coulometric titration measurements (dashed lines). (Reprinted with permission. ©2012 Elsevier).

was designed as a reference electrode for use with Ca^{2+} -bearing molten salt electrolytes [8].

2. Experimental section

2.1. Materials preparation

All materials were prepared in an inert argon atmosphere glovebox (O_2 concentration < 1 ppm). High-purity anhydrous salts of LiCl (99.995%, Alfa Aesar, Stock No. 13684), NaCl (99.99%, Alfa Aesar, Stock No. 35716), CaCl_2 (99.99%, Alfa Aesar, Stock No. 44280) and BaCl_2 (99.998%, Alfa Aesar, Stock No. 13686) were used to make 38–27–35 mol% LiCl–NaCl– CaCl_2 and 29–20–35–16 mol% LiCl–NaCl– CaCl_2 – BaCl_2 molten salt electrolytes. The salts were weighed out in appropriate quantities in ~500 g batches, mixed, and placed into a quartz crucible (Technical Glass Products). The crucible was then inserted into a stainless steel vacuum chamber, the chamber sealed, and loaded into a crucible furnace. To prepare dry, homogenous molten salt electrolytes the test chamber was 1) evacuated to ~1 Pa; 2) heated at 80 °C for 12 h under vacuum; 3) heated

at 230 °C for 12 h under vacuum; 4) purged with $\sim 0.2 \text{ cm}^3 \text{ s}^{-1}$ ultra-high purity argon gas (99.999%, O_2 < 1 ppm H_2O < 1 ppm, Airgas Inc.); and 5) heated at 700 °C for 3 h under flowing argon gas. After cooling to room temperature, the pre-melted electrolyte was transferred back to the glovebox and ground into a fine powder.

Electrodes were prepared from pure calcium (99.99%, Aldrich, Stock No. 441872) and bismuth (99.999%, Alfa Aesar, Stock No. 14442). The reference electrode (RE) comprised of a Ca–Bi alloy ($x_{\text{Ca}} = 0.35$) was prepared by arc-melting (MAM1, Edmund Bühler GmbH) pure calcium and bismuth metal together to form a homogeneous alloy and then transferred to a glovebox. Using an induction heater (MTI Corporation, EQ-SP-15A), custom-installed inside the glovebox, ~4 g samples of the arc-melted Ca–Bi alloys ($x_{\text{Ca}} = 0.35$) were re-melted inside BN crucibles (Saint-Gobain Advanced Ceramics, Product No. AX05). The approximate dimensions of the reference electrode's BN crucible were as follows: 12 mm outer diameter, 8 mm inner diameter, 19 mm height, and 15 mm depth. The counter electrode (CE) was also prepared in a BN crucible by induction melting pure bismuth and then gradually adding calcium metal until a calcium composition of $x_{\text{Ca}} = 0.15$ was achieved. A larger counter electrode area (eight times greater than the working electrode) was selected to offer facile transfer kinetics. The approximate dimensions for the counter electrode's BN crucible were as follows: 25 mm outer diameter, 21 mm inner diameter, 22 mm height, and 20 mm depth. Similarly, working electrodes (WEs) were prepared by induction melting pure bismuth in a BN crucible with inner diameters between 6 mm and 8 mm.

A capillary reference electrode was used for several experiments and constructed from the reference electrode describe above, where a 0.5 mm hole was drilled in the sidewall of the BN crucible at a position located between the top of the Ca–Bi alloy and the top of the crucible. When using the capillary reference electrode, upon assembly the electrode was carefully positioned within the electrolyte such that the electrolyte level was above the capillary hole and below the top of the reference electrode crucible.

2.2. Electrochemical cell assembly

The electrochemical cell components were assembled in an inert argon atmosphere glovebox (O_2 concentration < 1 ppm). Electrical contact was made with the electrodes using a tungsten

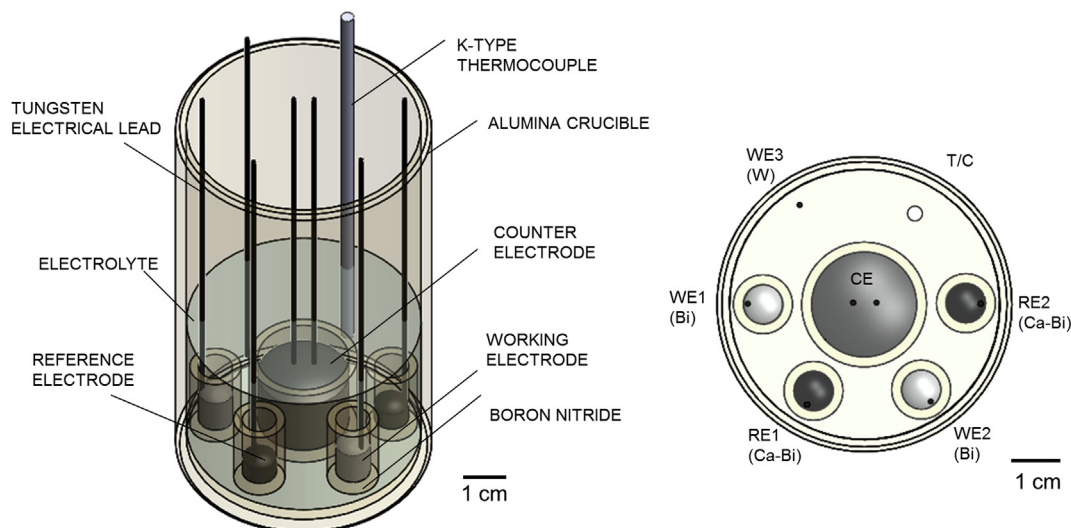


Fig. 2. Schematic of the electrochemical set-up designating the position of the working electrodes (WEs), reference electrodes (REs), counter electrode (CE), and thermocouple (T/C).

wire (Alfa Aesar, Stock No. 10411), approximately 1 mm in diameter and 47 cm in length; which were inserted into each electrode during induction melting. Each electrical lead was insulated from the test vessel using an alumina tube. The electrodes were arranged inside an alumina crucible with 56 mm inside diameter and 100 mm height and then ~140 g electrolyte was added over them. The final electrochemical cell configuration, as shown in Fig. 2, was then placed into a stainless steel vacuum chamber, the chamber sealed, and loaded into a crucible furnace.

2.3. Electrochemical measurements

In order to study the electrochemical behavior of a single electrode, a standard three-electrode setup (Fig. 2) was used for all electrochemical measurements; where the current is applied between the working and counter electrodes; while the voltage is measured between the working and reference electrodes ($E_{\text{cell}} = E_{\text{WE}} - E_{\text{RE}}$). Literature values of the equilibrium electrode potentials versus Ca(s) for the selected Ca–Bi alloy ($x_{\text{Ca}} = 0.35$) reference electrode (Table 2) were used to calculate the reported working electrode potentials E_{WE} versus Ca(s). Going forward the following simplified notation for the reported working electrode potentials is used: E_{WE}/V versus Ca(s) $\rightarrow E/\text{V}$.

Before each electrochemical measurement, cells were heated in the sealed test chamber at 80 °C and 230 °C under vacuum for 12 h each to remove residual moisture and oxygen gas, and then heated to a starting temperature of 600 °C at a heating rate of 5 °C min⁻¹ under ~0.2 cm³ s⁻¹ flowing ultra-high purity argon gas. The cell temperature was monitored using a type-K thermocouple and voltage difference between the two reference electrodes collected using a data acquisition board (National Instruments, NI 9211). All electrochemical measurements were made using a potentiostat–galvanostat (Metrohm AG, PGSTAT302N) and frequency response analyzer (Metrohm AG, FRA32M).

The stability and consistency of the selected reference electrode was verified by a drift in electrode potential (dE_{RE}/dt) of less than 20 $\mu\text{V h}^{-1}$ and a difference between the two Ca–Bi reference electrodes ($E_{\text{RE1}} - E_{\text{RE2}}$) less than 0.2 mV at temperatures of 500–700 °C, as shown in Fig. 3.

2.3.1. Coulometric titration

At the beginning of each coulometric titration measurement, the pure bismuth working electrodes were held at 1.5 V for 1 h to insure consistent initial conditions. The composition of the working electrode was then varied by electrochemically titrating calcium for a time $t = 5000$ – 6000 s at a constant current density $j = \pm 50$ – 100 mA cm⁻², while recording the electrode potential. Each titration step was followed by an open circuit measurement for 5000–6000 s to allow the electrode composition to homogenize. Experiments were performed at temperatures of 500, 600, and 700 °C.

Assuming perfect coulombic efficiency for calcium titration, the calcium mole fraction x_{Ca} was estimated by:

$$x_{\text{Ca}} = \left(1 + \frac{m_{\text{Bi}} z F}{M_{\text{Bi}} j A t} \right)^{-1} \quad (9)$$

Table 2
Equilibrium electrode potentials of Ca–Bi ($x_{\text{Ca}} = 0.35$) versus Ca(s) [8].

E_{eq}/V	$T/^{\circ}\text{C}$
0.806	500
0.785	600
0.765	700

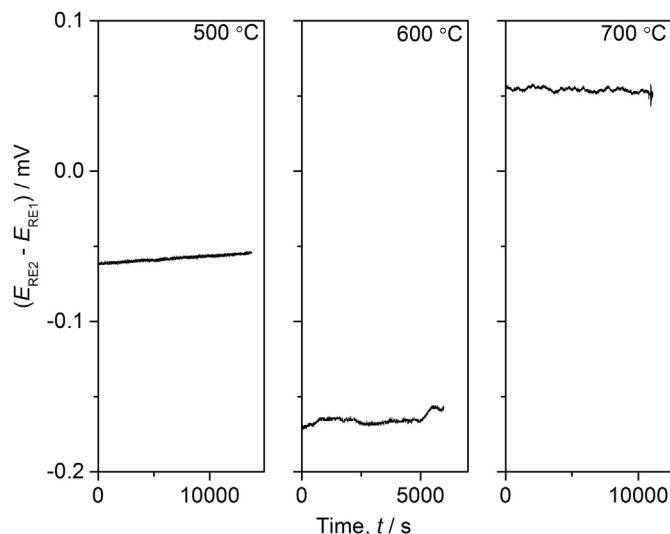


Fig. 3. The potential difference between two Ca–Bi alloy ($x_{\text{Ca}} = 0.35$) reference electrodes ($E_{\text{RE2}} - E_{\text{RE1}}$) as a function of time in a LiCl–NaCl–CaCl₂ electrolyte.

where the mass of bismuth $m_{\text{Bi}} = 3.43$ g, the molecular weight of bismuth $M_{\text{Bi}} = 209$ g mol⁻¹, and the working electrode area $A = 0.50$ cm².

2.3.2. Cyclic voltammetry

The electrochemical window of the LiCl–NaCl–CaCl₂ electrolyte was measured from -0.1 V to 4.0 V versus Ca(s) at 600 °C by cyclic voltammetry at scan rates of 0.05 – 0.20 V s⁻¹. Three different three-electrode setups were used as given in Table 3.

2.3.3. Electrochemical impedance spectroscopy

Electrochemical impedance spectroscopy (EIS) was used to probe the electrode behavior of the cells at 600 °C using a capillary reference electrode. Impedance spectra collected from an applied 5 mV amplitude over 10 mHz–0.1 MHz frequency range were fit to a $RL(Q(RW))$ equivalent circuit model, where R is a resistor, L is an inductor, Q is a constant phase element, and W is a Warburg diffusion element.

2.3.4. Tafel analysis

Tafel analysis was performed on data collected using a capillary reference electrode and a linear polarization sweep at 50 mV s⁻¹ for several compositions at different starting equilibrium electrode potentials E_{eq} upon calcium deposition and removal. Data was IR -corrected using the ohmic resistance R_{ohm} measured by impedance spectroscopy and the logarithm of current density $\log |j|$ plotted as a function of overpotential $\eta = E - E_{\text{eq}} - jAR_{\text{ohm}}$.

2.4. Post-mortem analysis

At the end of each experiment, electrodes were coulometrically titrated to a target calcium concentration and cooled to room

Table 3
Three-electrode setups for cyclic voltammetry measurements.

Setup	WE	CE	RE	Electrolyte
1	W	W	Ca–Bi ($x_{\text{Ca}} = 0.35$) ^a	LiCl–NaCl–CaCl ₂
2	W	Ca–Bi ($x_{\text{Ca}} = 0.15$)	Ca–Bi ($x_{\text{Ca}} = 0.35$) ^a	LiCl–NaCl–CaCl ₂
3	Bi	Ca–Bi ($x_{\text{Ca}} = 0.15$)	Ca–Bi ($x_{\text{Ca}} = 0.35$)	LiCl–NaCl–CaCl ₂

^a Capillary reference electrode. Working electrode (WE), counter electrode (CE), reference electrode (RE).

temperature for post-mortem analysis. The electrodes were mounted in epoxy, carefully cross-sectioned, polished using silicon carbide abrasive paper up to 1500 grit, and ultrasonically cleaned in isopropyl alcohol. Cross-sectioned electrodes were first optically

examined using a stereomicroscope (Olympus SZ61). After optical examination, a scanning electron microscope (JEOL 6610LV) fitted with an energy dispersive spectrometer (IXRF systems, Model 55i) was used for qualitative chemical analysis.

3. Results and discussion

3.1. Electrochemical window

Using an electrochemical set-up shown in Fig. 2, the potential window of the molten salt electrolyte with and without Ca–Bi electrodes was examined to identify faradaic processes. From the cyclic voltammetry data collected using inert tungsten working and counter electrodes in LiCl–NaCl–CaCl₂ at 600 °C, presented in Fig. 4a, calcium metal is deposited and removed from the working electrode near 0.0 V, and chlorine gas begins to evolve at electrode potentials greater than 3.5 V.

However, when a Ca–Bi ($x_{\text{Ca}} = 0.15$) counter electrode was introduced, Fig. 4b (dotted lines), a distinct faradaic process is observed at about 0.78 V, while none is observed for tungsten electrodes (solid lines) between 0.6 V and 1.6 V. We propose that this process is the result of calcium dissolution from the Ca–Bi counter electrode to form subvalent calcium ions,

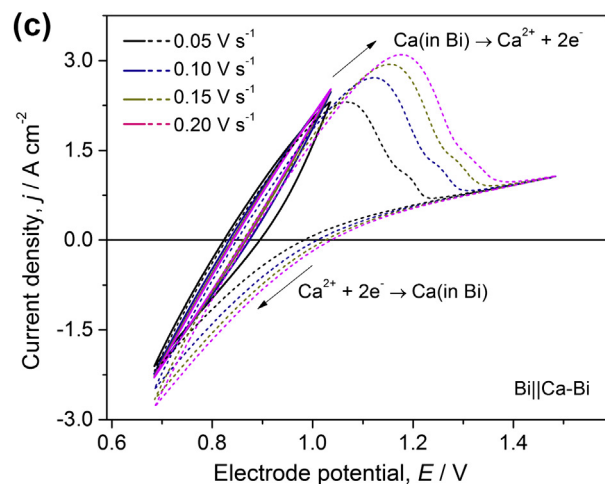
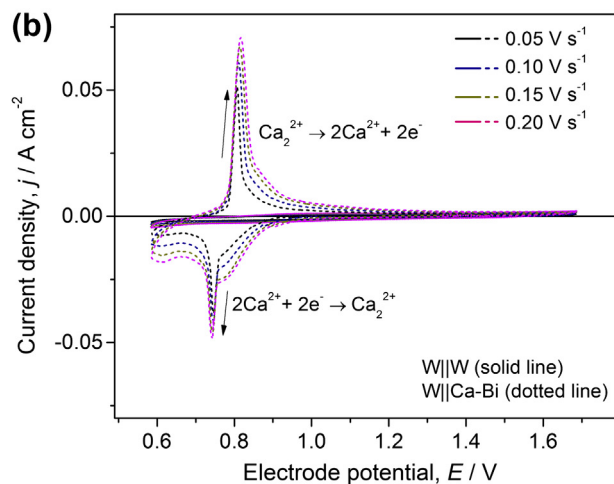
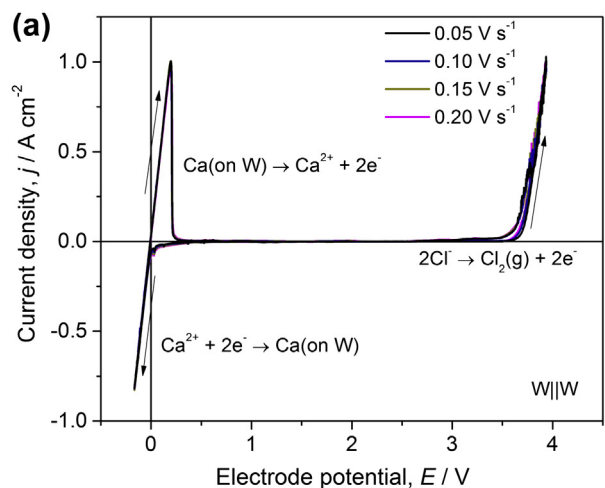


Fig. 4. Cyclic voltammograms at 600 °C in a LiCl–NaCl–CaCl₂ electrolyte at scan rates of 0.05–0.20 V s^{−1} using (a) only tungsten electrodes with a capillary Ca–Bi ($x_{\text{Ca}} = 0.35$) reference electrode; (b) only tungsten electrodes (solid line) and tungsten with Ca–Bi ($x_{\text{Ca}} = 0.15$) counter electrode (dotted line) and capillary Ca–Bi ($x_{\text{Ca}} = 0.35$) reference electrode; and (c) a pure bismuth working electrode with Ca–Bi ($x_{\text{Ca}} = 0.15$) counter electrode and a normal Ca–Bi ($x_{\text{Ca}} = 0.35$) reference electrode.

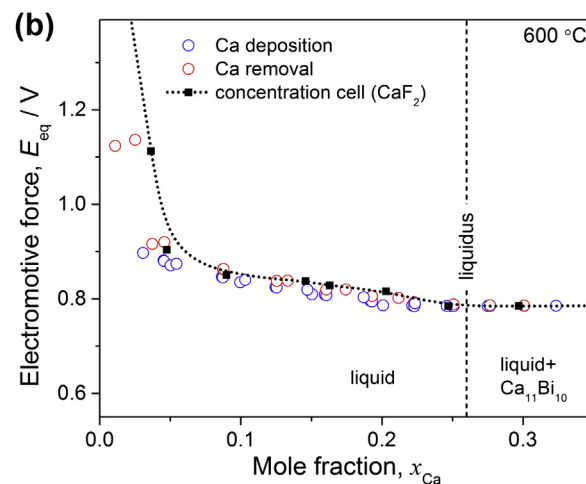
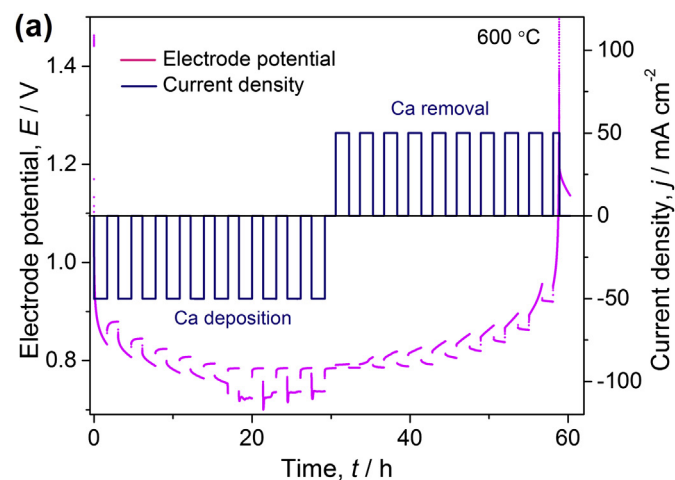
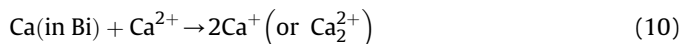


Fig. 5. (a) Coulometric titration of calcium to and from liquid bismuth working electrode in a LiCl–NaCl–CaCl₂ electrolyte at 600 °C at current densities of ± 50 mA cm^{−2} followed by an open circuit measurement. (b) Coulometric titration emf data as a function of mole fraction x_{Ca} upon calcium deposition and removal compared to concentration cell data [8] at 600 °C.

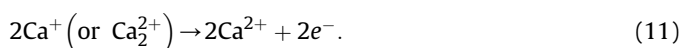
Table 4

Equilibrium potentials of Ca–Bi alloys [in V versus Ca(s)] from coulometric titration (this work) and concentration cell measurements [8].

x_{Ca}	500 °C		600 °C		700 °C	
	This work	Ref. [8]	This work	Ref. [8]	This work	Ref. [8]
0.04	0.870	1.070	0.916	1.113	0.909	1.155
0.05	0.861	0.886	0.885	0.903	0.904	0.922
0.09	0.835	0.839	0.852	0.850	0.856	0.861
0.15	0.821	0.832	0.819	0.837	0.829	0.835
0.20	–	0.814	0.786	0.816	0.787	0.818
0.25	–	0.807	0.786	0.784	0.787	0.788
0.30	–	0.806	0.785	0.785	0.766	0.768



followed by an electrochemical reaction to form calcium ions,



Consistent with this hypothesis are the relatively low current densities observed (less than 50 mA cm^{-2}); which would indicate low concentrations of calcium subvalent ions. Future validation will likely require optical spectroscopy to identify the formation of subvalent ionic species and is beyond the scope of this work.

When using a pure bismuth working electrode, the drop in current density observed above 1.2 V, Fig. 4c (dotted lines), suggests the supply of calcium in the working electrode is exhausted and the oxidative reaction $[\text{Ca(in Bi)} \rightarrow \text{Ca}^{2+} + 2e^-]$ is mass transport limited, which stands in contrast to the near linear behavior observed at potentials between 0.7 V and 1.2 V, Fig. 4c (solid lines).

3.2. Thermodynamic behavior

The accuracy of the coulometric titration data using molten salt electrolytes for Ca–Bi alloys collected in this work is compared against previously reported thermodynamic results obtained using a concentration cell with a CaF_2 solid electrolyte [8]. Representative coulometric titration emf data upon calcium deposition and removal at 600 °C are presented in Fig. 5a. From the open circuit measurement following each titration, the equilibrium electrode potentials as function of calcium mole fraction are extracted and compared with previous concentration cell measurements in Fig. 5b and Table 4. The emf values between the two different methods are generally in good agreement and especially consistent within the liquid + $\text{Ca}_{11}\text{Bi}_{10}$ two-phase domain, with a difference of less than 2 mV. However, in dilute solutions of Ca–Bi alloys ($x_{\text{Ca}} < 0.05$) the discrepancies between the two methods are as high as 200 mV due to the combined effects of a steep change in emf as the electrode approaches infinite dilution and the small amount of

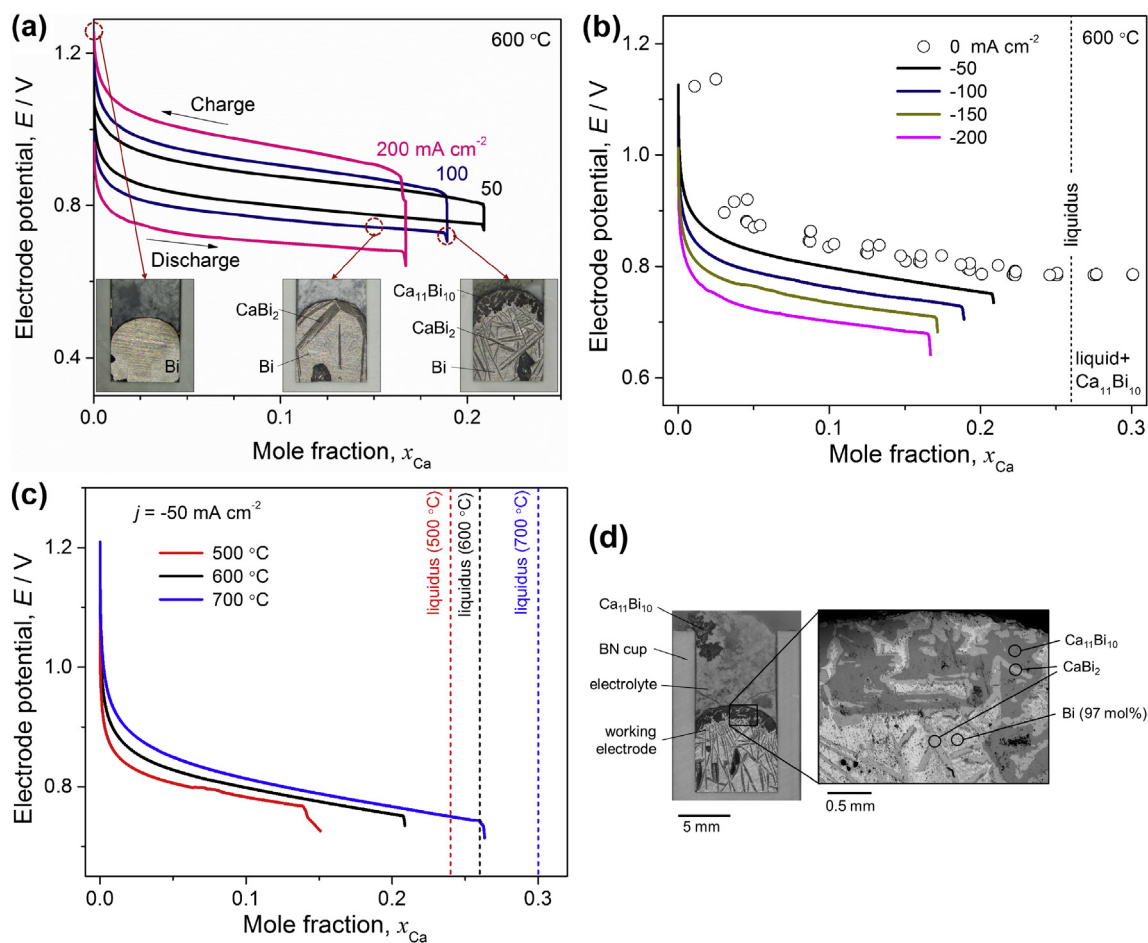


Fig. 6. (a) Charge-discharge cycles of liquid bismuth electrode in LiCl-NaCl-CaCl_2 at 600 °C with the post-mortem images of Ca–Bi alloys at different states of discharge. Electrode potential upon calcium deposition into liquid bismuth as a function of calcium mole fraction (b) at current densities of (0, -50, -100, -150, -200) mA cm^{-2} and 600 °C, and (c) at temperatures of (500, 600, 700) °C and -50 mA cm^{-2} . (d) Post-mortem analysis of a bismuth electrode after calcium deposition to a calcium mole fraction of $x_{\text{Ca}} \sim 0.18$ at a current density of -150 mA cm^{-2} from a LiCl-NaCl-CaCl_2 electrolyte at 600 °C.

self-discharge caused by calcium dissolution from the Ca–Bi counter electrode.

3.3. Kinetic behavior

The liquid bismuth electrodes were tested by charge–discharge cycling at constant current densities up to 200 mA cm^{-2} at 600°C (Fig. 6a). These electrodes exhibited high coulombic efficiencies $>98\%$, indicating chemically reversible electrode reactions and experienced lower discharge capacity at higher current densities with a sharp decrease in the electrode potential near the end of discharge. The post-mortem analyses of Ca–Bi alloys at different states of discharge (Fig. 6a) indicate that this sharp electrode potential decrease originates from the nucleation of solid phase at the electrode–electrolyte interface (nucleation overpotential).

3.3.1. Intermetallic layer formation

The nucleation of the solid intermetallic $\text{Ca}_{11}\text{Bi}_{10}$ phase at the electrode–electrolyte interface as the electrode composition approaches the liquidus (liquid = liquid + $\text{Ca}_{11}\text{Bi}_{10}$) during calcium deposition causes the sharp decrease in the cell potential that is observed in Fig. 5a ($15 \text{ h} < t < 30 \text{ h}$). This is corroborated by the results presented in Fig. 6b, where the drop in electrode potential

occurs at successively lower calcium concentrations as the deposition current density is increased from 50 mA cm^{-2} – 200 mA cm^{-2} . The nucleation of a non-equilibrium $\text{Ca}_{11}\text{Bi}_{10}$ intermetallic phase at the electrode–electrolyte interface and steep drop in electrode potential at high current densities can be explained, in part, by a calcium diffusion rate into the bismuth electrode that is slower than the rate of calcium deposition. As one might expect for a kinetically derived diffusion process, this behavior is accentuated by reducing the cell temperature from 700°C to 500°C , Fig. 6c.

Post-mortem analysis of electrodes quenched to room temperature after deep discharging to a composition of $x_{\text{Ca}} \sim 0.18$, ($j = -150 \text{ mA cm}^{-2}$, 600°C) revealed a high concentration of the low density $\text{Ca}_{11}\text{Bi}_{10}$ intermetallic at the electrode–electrolyte interface, Fig. 6d. This effect is encouraged by a significant difference in density between $\text{Ca}_{11}\text{Bi}_{10}$ ($\sim 6.33 \text{ g cm}^{-3}$) and molten bismuth ($\sim 9.78 \text{ g cm}^{-3}$). Further investigation of post-mortem samples also found $\text{Ca}_{11}\text{Bi}_{10}$ dendrites mixed with electrolyte salt situated above, and completely detached from, the bulk electrode, Fig. 6d. The separation of the dendrites is thought to come from the convective motion of the molten electrolyte. The formation and separation of $\text{Ca}_{11}\text{Bi}_{10}$ dendrites from the bulk electrode would explain the often erratic voltage profiles observed at high rates of calcium deposition and high calcium concentrations (Fig. 5a),

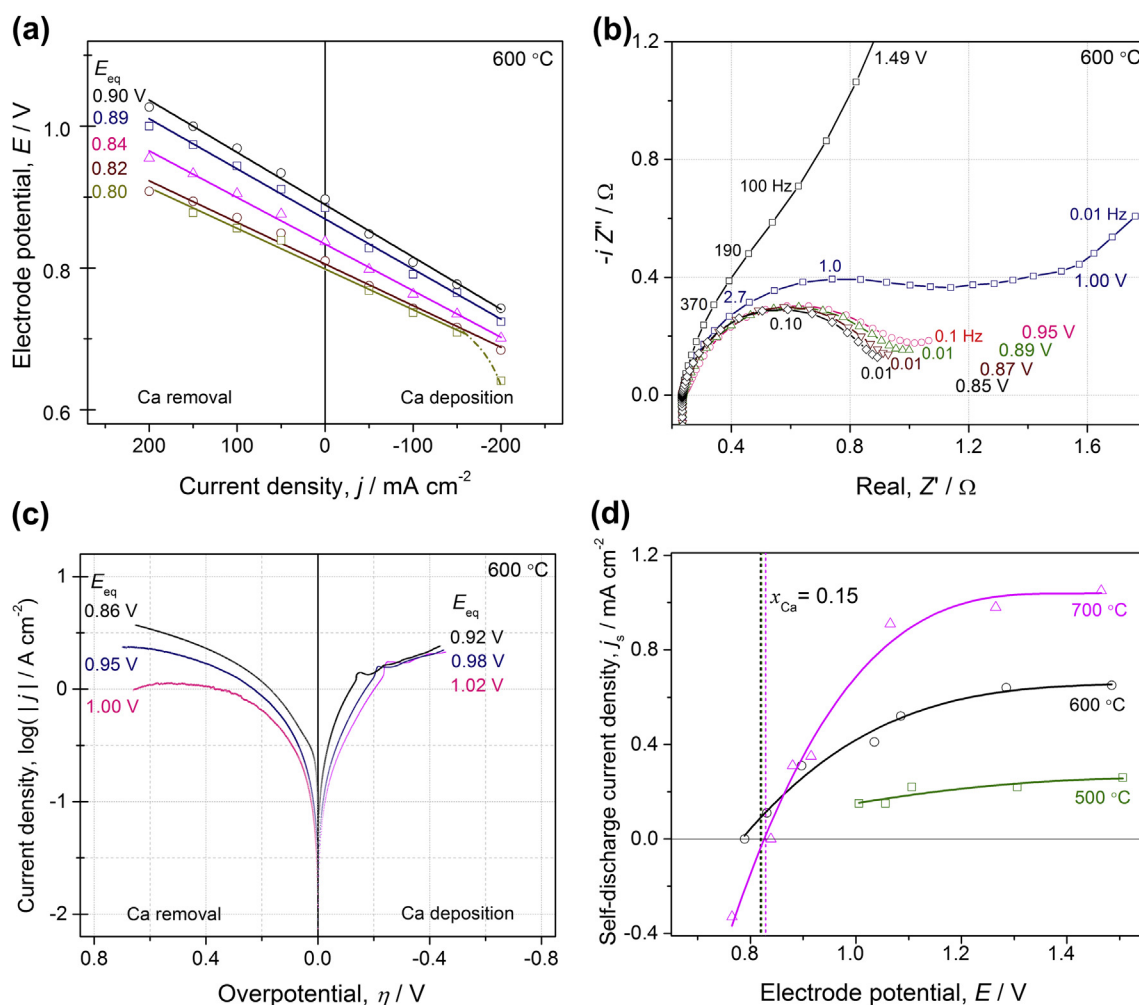


Fig. 7. For a Ca–Bi electrode at various equilibrium electrode potentials (compositions) in a LiCl–NaCl–CaCl₂ electrolyte: (a) polarization curves upon calcium deposition and removal, (b) Nyquist plots, (c) Tafel plots upon calcium deposition and removal at 600°C , and (d) self-discharge current densities as a function of electrode potential of a Ca–Bi electrode at $(500, 600, 700)^\circ\text{C}$.

which can also lead to a loss in coulombic capacity and a short in the cell.

3.3.2. Voltage inefficiencies

The measured electrode potential deviates from the equilibrium potential due to current density dependent overpotentials ($\eta = E - E_{eq}$) that result from charge transfer, ohmic, and mass transport losses. Polarization curves are presented in Fig. 7a for different equilibrium electrode potentials ($E_{eq} = 0.80$ – 0.90 V) upon calcium deposition and removal at 600°C . The slope of each polarization curve is equal to the total area specific resistance $A \cdot R_{tot}$ for each equilibrium electrode potential and these values are given in Table 5. From these results, the total area specific resistance is observed to decrease from about $0.74 \Omega \text{ cm}^2$ to $0.58 \Omega \text{ cm}^2$ upon reducing the equilibrium electrode potential.

To separate out relative contributions to the total electrode resistance by charge transfer, ohmic, and mass transport losses, electrochemical impedance spectra were collected at equilibrium electrode potentials from 1.00 V to 0.85 V at 600°C , Fig. 7b. From the equivalent circuit model fitting results presented in Table 6, the ohmic resistances R_{ohm} (the high frequency semi-circle intercept) and the charge transfer resistances R_{ct} (the semi-circle width) were estimated. As is typical for a three-electrode setup, the area specific ohmic resistance $A \cdot R_{ohm}$ contribution was small ($\sim 0.07 \Omega \text{ cm}^2$) and independent of the equilibrium electrode potential. By contrast, the area specific charge transfer resistance $A \cdot R_{ct}$ decreased substantially upon decreasing the equilibrium electrode potential, from $0.27 \Omega \text{ cm}^2$ to $0.18 \Omega \text{ cm}^2$. Based on these results, a Ca–Bi electrode at 0.89 V and 600°C has a total area specific resistance of $\sim 0.71 \Omega \text{ cm}^2$ (Table 5); which is comprised of about 31% ($0.20 \Omega \text{ cm}^2$) charge transfer resistance and 10% ($0.07 \Omega \text{ cm}^2$) ohmic resistance (Table 6), with the majority of remaining losses attributable to mass transport limitations ($R_{mt} = R_{tot} - R_{ct} - R_{ohm}$).

The nature of the charge transfer kinetics in this system is revealed in the values of electrode exchange current densities j_0 estimated from Tafel plots (Fig. 7c) at equilibrium potentials from 0.86 V to 1.00 V and 600°C for calcium deposition and removal. While ideal Tafel behavior was not observed due to mass transport limitations, approximate values were obtained for the exchange current density, and the results are reported in Table 7. During calcium removal, the exchange current density increased from 0.14 A cm^{-2} to 0.27 A cm^{-2} as the equilibrium electrode potential was decreased from 1.00 V to 0.86 V and similar values were obtained for calcium deposition. These results are in excellent agreement with the EIS data presented in Table 6, where the exchange current density was estimated from Ref. [15]

$$j_0 = RT/zFAR_{ct}. \quad (12)$$

The Tafel plots also reveal significant asymmetry between calcium deposition and removal, Fig. 7c. The calcium removal traces are smooth and yield Tafel slopes of $-(0.26$ – $0.29) \text{ V dec}^{-1}$, while calcium deposition profiles are irregular at more negative overpotentials with Tafel slopes of $\sim 0.20 \text{ V dec}^{-1}$. The erratic deposition

Table 6

Equivalent circuit model $RL(Q(RW))$ fit results to the electrochemical impedance spectra of Ca–Bi electrodes at 600°C .

E_{eq}/V	$A \cdot R_{ohm}/\Omega \text{ cm}^2$	$L/\mu\text{H}$	$A \cdot R_{ct}/\Omega \text{ cm}^2$	A_W/Ω	Y_0/Ω^{-1}	n	χ^2	$j_0/\text{A cm}^{-2}$
1.00	0.07	0.44	0.27	0.23	0.20	0.85	0.02	0.14
0.95	0.07	0.42	0.21	0.13	0.13	0.83	0.02	0.18
0.89	0.07	0.40	0.20	0.04	1.04	0.86	0.00	0.19
0.87	0.07	0.40	0.19	0.02	1.62	0.90	0.00	0.20
0.85	0.07	0.44	0.18	0.02	2.08	0.92	0.00	0.21

Exchange current density j_0 estimated from $j_0 = RT/zFAR_{ct}$. $W = A_W(i\omega)^{-0.5}$
 $Q = Y_0(i\omega)^n$. $A = 0.28 \text{ cm}^2$.

behavior was likely caused by the formation of Ca–Bi intermetallics at the electrode–electrolyte interface, as previously discussed.

3.3.3. Coulombic inefficiencies

In an electrochemical system, non-faradaic inefficiencies comprised of capacitive, electrical, and chemical losses can either 1) reduce electrode capacity over time (dQ/dt) if the system is held at open circuit potential, or 2) generate a self-discharge current density j_s if the system is held at a constant electrode potential. In a sense, these galvanic losses can be thought of as chemical and electrical short-circuits and are different from overpotential losses, which are current density dependent and result in voltage inefficiencies. Galvanic losses are electrode potential dependent and result in coulombic inefficiencies.

Self-discharge current densities j_s at 500 – 700°C were measured using a LiCl–NaCl–CaCl₂ electrolyte, while holding at discrete electrode potentials between 0.77 V and 1.50 V. From the results plotted in Fig. 7d, a couple of trends are apparent. First, elevated temperatures lead to higher self-discharge current densities. For example, at an electrode potential of ~ 1.1 V the self-discharge current density is only 0.2 mA cm^{-2} at 500°C , but over 0.9 mA cm^{-2} at 700°C . Second, as the applied working electrode potential nears ~ 0.83 V, which corresponds to the counter electrode potential ($x_{Ca} = 0.15$), the self-discharge current density drops to zero.

3.4. Barium co-deposition

Based upon the original work by Argonne National Laboratory on calcium–iron sulfide batteries, in this investigation the initial choice of electrolyte for studying the kinetics of liquid Ca–Bi alloy electrodes was the low melting LiCl–NaCl–CaCl₂–BaCl₂ melt. However, post-mortem analysis of the electrodes revealed the presence of a 9–33–58 mol% Ca–Ba–Bi alloy phase (Fig. 8a) which was taken as an indication of co-deposition of barium.

Closer examination of the Ca–Bi and Ba–Bi binary phase diagrams [16,17] confirms that barium is found to have a higher solubility in bismuth than calcium at 600°C ($x_{Ba} = 0.30$ compared to $x_{Ca} = 0.26$) and fewer intermetallic compounds, see Table 8. Moreover, higher capacity discharge profiles were obtained with the addition of BaCl₂ in the molten salt electrolyte, Fig. 8b. These results can be explained by 1) the higher solubility of barium in

Table 5

Total area specific resistance ($A = 0.50 \text{ cm}^2$) of a Ca–Bi electrode at a given calcium mole fraction/equilibrium electrode potential at 600°C .

E_{eq}/V	x_{Ca}	$A \cdot R_{tot}/\Omega \text{ cm}^2$
0.90	0.03	0.74
0.89	0.05	0.71
0.84	0.10	0.66
0.82	0.15	0.59
0.80	0.17	0.58

Table 7

Tafel results from a linear fit of overpotentials of 60 – 170 mV.

	E_{eq}/V	$j_0/\text{A cm}^{-2}$	Tafel slope/ V dec^{-1}
Ca removal	1.00	0.14	–0.28
	0.95	0.18	–0.26
	0.86	0.27	–0.29
Ca deposition	1.02	0.12	0.20
	0.98	0.15	0.20
	0.92	0.26	0.20

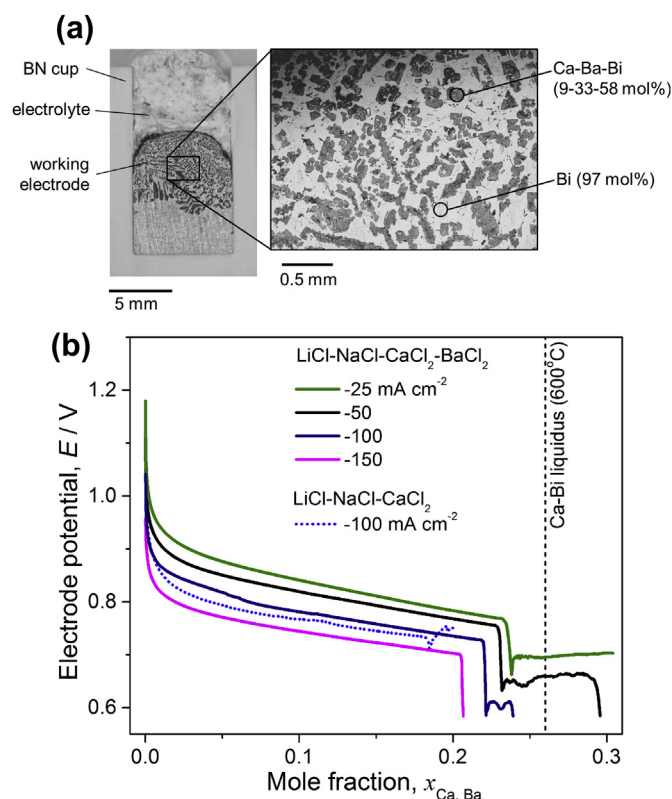


Fig. 8. (a) Post-mortem analysis of a bismuth electrode after calcium/barium deposition to a mole fraction of $x_{\text{Ca,Ba}} \sim 0.10$ at a current density of -100 mA cm^{-2} from a $\text{LiCl-NaCl-CaCl}_2\text{-BaCl}_2$ electrolyte at 600°C . (b) Electrode potential upon calcium/barium deposition into liquid bismuth at current densities of $-(25\text{--}150) \text{ mA cm}^{-2}$ from a $\text{LiCl-NaCl-CaCl}_2\text{-BaCl}_2$ electrolyte at 600°C as a function of calcium/barium mole fraction.

bismuth, 2) the notable absence of lower concentration intermetallic phases in the barium–bismuth system (Ba_5Bi_3 , $x_{\text{Bi}} = 0.63$) compared to the calcium–bismuth system ($\text{Ca}_{11}\text{Bi}_{10}$, $x_{\text{Ca}} = 0.52$) at temperature of 500°C – 700°C , and 3) the higher density of barium–bismuth compounds (Table 8), which should promote the removal of intermetallic products from the electrode–electrolyte interface.

Based upon the known deposition potentials for pure metals from metal chloride salts [$\text{M}^{+z} + z\text{e}^- \rightarrow \text{M}(\text{s})$], the expected order of deposition is $\text{Ca} \rightarrow \text{Na} \rightarrow \text{Li} \rightarrow \text{Ba}$ [18]. However, when the activity of the metal in bismuth $a_{\text{M}(\text{in Bi})}$ is considered at low concentrations ($x_{\text{M}(\text{in Bi})} < 0.1$) the expected order of metal deposition looks

Table 8

Densities of pure elements and intermetallic compounds in the Ca–Bi and Ba–Bi systems [16,17].

	$\rho/\text{g cm}^{-3}$	$T/^\circ\text{C}$
Ca(s)	1.55	25
Ca(l)	1.38	842
CaBi ₂	8.34	25
Ca ₁₁ Bi ₁₀	6.33	25
Ca ₁₆ Bi ₁₁	5.47	25
Ca ₅ Bi ₃	5.30	25
Ba(s)	3.51	25
Ba(l)	3.34	727
BaBi ₃	9.14	25
Ba ₅ Bi ₃	6.30	25
Bi(s)	9.78	25
Bi(l)	10.05	271

Table 9

Equilibrium electrode potentials for the deposition of metals $\text{M} = \text{Li}, \text{Na}, \text{Ca}$, and Ba onto an inert electrode from a metal chloride molten salt MCl_z ($z = 1, 2$) compared to the deposition of metals M into a bismuth electrode ($x_{\text{M}} = 0.10$) at 600°C for Li–Bi [20], Na–Bi [19], and Ca–Bi [8] alloys and at 850°C for Ba–Bi alloys [7].

M	$E_{\text{eq}}/\text{V}^{\text{a}}$	$E_{\text{eq}}/\text{V}^{\text{b}}$
Ba	−0.31	0.92
Ca	0.00	0.85
Li	−0.07	0.81
Na	−0.01	0.75

^a $E_{\text{eq}}^\circ (\text{M}^{z+}|\text{M})$ versus $\text{Ca}(\text{s})$.

^b $E_{\text{eq}} (\text{M}^{z+}|\text{M}(\text{in Bi}))$ versus $\text{Ca}(\text{s})$ at $x_{\text{M}} = 0.10$.

markedly different: $\text{Ba} \rightarrow \text{Ca} \rightarrow \text{Li} \rightarrow \text{Na}$ (Table 9 [7,8,19,20]). It should be noted that the high coulombic efficiencies (typically $> 98\%$) observed even when barium co-deposition was occurring indicate that the electrode reactions are reversible and therefore have utility in energy storage.

4. Conclusion

Calcium–bismuth liquid metal electrodes exhibit excellent reversibility, making Bi a promising positive electrode candidate for liquid metal batteries. The dissolution of calcium into molten salt electrolytes was suppressed by a combination of alloying of the electrode and use of a multi-cation electrolyte. A stable Ca–Bi alloy ($x_{\text{Ca}} = 0.35$) reference electrode enabled the evaluation of the electrode kinetics of liquid Ca–Bi alloys by coulometric titration, electrochemical impedance spectroscopy, and Tafel analysis. A self-discharge current density of less than 1 mA cm^{-2} allowed for accurate coulometric measurements and high coulombic efficiency $> 98\%$. Calcium–bismuth electrode exchange current densities of $\sim 200 \text{ mA cm}^{-2}$ were measured at electrode equilibrium potentials between 0.8 and 1.0 V versus $\text{Ca}(\text{s})$, while mass transport losses were found to dominate electrode overpotentials. The formation of intermetallic species at the electrode–electrolyte interface presents the greatest challenge to operating Ca–Bi electrodes at high current densities and suggests a mechanism for loss in capacity. The introduction of barium into the Ca–Bi electrode could be one strategy to minimize the formation of these Ca–Bi intermetallics and enhance electrode performance. Calcium–bismuth positive electrodes combined with the development of new negative electrode alloys with low calcium electrolyte solubility could lead to a promising liquid metal battery for electrochemical energy storage that relies on low cost, earth-abundant materials.

Author contributions

The manuscript was written through contributions of all authors. All authors have given approval to the final version of the manuscript.

Funding sources

US Department of Energy, Advanced Research Projects Agency-Energy (Award No. DE-AR0000047) and TOTAL, S.A.

Acknowledgment

The financial support of the US Department of Energy, Advanced Research Projects Agency-Energy (Award No. DE-AR0000047) and TOTAL, S.A. is gratefully acknowledged.

References

- [1] L.M. Vrana, Calcium and Calcium Alloys, in: Kirk-othmer Encyclopedia of Chemical Technology, John Wiley & Sons, Inc., 2000, pp. 1–10.
- [2] H. Kim, D.A. Boysen, J.M. Newhouse, B.L. Spatocco, B. Chung, P.J. Burke, D.J. Bradwell, K. Jiang, A.A. Tomaszowska, K. Wang, W. Wei, L.A. Ortiz, S.A. Barriga, S.M. Poizeau, D.R. Sadoway, Chem. Rev. 113 (2013) 2075–2099.
- [3] R.A. Guidotti, P. Masset, J. Power Sources 161 (2006) 1443–1449.
- [4] P.A. Nelson, D.L. Barney, R.K. Steunenberg, A.A. Chilenskas, E.C. Gay, J.E. Battles, F. Hornstra, W.E. Miller, M.F. Roche, H. Shimotake, R. Hudson, R.J. Rubischko, S. Sudar, High-performance Batteries for Electric-vehicle Propulsion and Stationary Energy Storage. ANL-78–94, Argonne National Laboratory, Chicago, 1978.
- [5] P.A. Nelson, D.L. Barney, R.K. Steunenberg, A.A. Chilenskas, E.C. Gay, J.E. Battles, F. Hornstra, W.E. Miller, D.R. Vissers, M.F. Roche, H. Shimotake, R. Hudson, R.J. Rubischko, S. Sudar, High-performance Batteries for Electric-vehicle Propulsion and Stationary Energy Storage. ANL-79–39, Argonne National Laboratory, Chicago, 1979.
- [6] D.L. Barney, M.F. Roche, S.K. Preto, L.E. Ross, N.C. Otto, F.J. Martino, Calcium/Metal Sulfide Battery Development Program. ANL-81-14, Argonne National Laboratory, Chicago, 1981.
- [7] J. Delcet, A. Delgado-Brune, J.J. Egan, in: Y.A. Chang, J.F. Smith (Eds.), Symposium on Calculation of Phase Diagrams and Thermochemistry of Alloy Phases, Metallurgical Society of AIME, Milwaukee, Wisconsin, 1979, pp. 275–287.
- [8] H. Kim, D.A. Boysen, D.J. Bradwell, B. Chung, K. Jiang, A.A. Tomaszowska, K. Wang, W. Wei, D.R. Sadoway, Electrochim. Acta 60 (2012) 154–162.
- [9] T. Baak, J. Chem. Phys. 29 (1958), 1195–1195.
- [10] R.A. Sharma, J. Phys. Chem. 74 (1970) 3896–3900.
- [11] A.S. Dworkin, M.A. Bredig, H.R. Bronstein, Discuss. Faraday Soc. (1961) 188–196.
- [12] E.A. Ukshe, N.G. Bukun, Russ. Chem. Rev. 30 (1961) 90–107.
- [13] M.A. Bredig, Mixtures of Metals with Molten Salts. ORNL-3391, Oak Ridge National Laboratory, Oak Ridge, Tennessee, 1963.
- [14] C.J. Wen, B.A. Boukamp, R.A. Huggins, W. Weppner, J. Electrochem. Soc. 126 (1979) 2258–2266.
- [15] A.J. Bard, L.R. Faulkner, Electrochemical Methods: Fundamentals and Applications, John Wiley, New York, 2001.
- [16] T.B. Massalski, Binary Alloy Phase Diagrams, ASM International, Materials Park, Ohio, 1990.
- [17] CRC Handbook of Chemistry and Physics, 92nd ed., CRC Press, Cleveland, Ohio, 2012.
- [18] T.a. GTT-technologies, in, Thermfact and GTT-technologies, 2009.
- [19] E.J. Cairns, C.E. Crouthamel, A.K. Fischer, M.S. Foster, J.C. Hesson, Galvanic Cells with Fused Salts. ANL-7316, Argonne National Laboratory, Chicago, 1967.
- [20] W. Weppner, R.A. Huggins, J. Electrochem. Soc. 125 (1978) 7–14.